Chemical Geology 627 (2023) 121397

Contents lists available at ScienceDirect

Chemical Geology

journal homepage: www.elsevier.com/locate/chemgeo

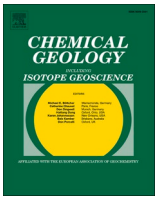

Pore merging and flow focusing: Comparative study of undissolved and karstified limestone based on microtomography

Rishabh P. Sharma [a], Mariusz Białecki [b], Max P. Cooper [a], Andrzej P. Radliński [a,c], Piotr Szymczak [a,*]

[a] Institute of Theoretical Physics, Faculty of Physics, University of Warsaw, Poland
[b] Institute of Geophysics, Polish Academy of Sciences, Warsaw, Poland
[c] University of New South Wales, School of Minerals and Energy Resources Engineering, Sydney, Australia

ARTICLE INFO

Edited by Dr. Karen Johannesson

Keywords:
Dissolution
Karst
Microtomography
Reactive area
Flow focusing
Pore space evolution

ABSTRACT

We develop methods for qualitative and quantitative assessment of pore geometry transformation within a rock as a result of karstification. We then apply these tools to characterize dissolution-induced changes in limestone samples collected from a quarry in Smerdyna (Poland), where intense epikarst development is observed, consisting of a large number of solution pipes. Partially dissolved samples collected in the immediate vicinity of the pipes were compared with undissolved samples collected 1.5 meters away. For both types of samples 26 micron resolution grayscale X-ray scans were performed. The irregular geometry of the pore space, the vast majority of which forms a single connected component, can be conveniently characterized by a local thickness function that corresponds to the diameter of the largest sphere that fits within the pore space and contains a given point. We compare the local thickness distributions of the undissolved and dissolved samples as well as a numerically generated uniformly dissolved sample. Such a comparison allows us to quantify the extent of homogeneity of the natural karstification process. The above analysis is complemented by the calculation of connectivity of the pore space as well as their flow characteristics. All of the results consistently indicate an important role of pore merging and inhomogeneous dissolution in the process of natural dissolution for the analyzed samples.

1. Introduction

The high solubility of carbonate minerals allows for the development of secondary porosity, enlarging fractures and transforming them into caves and karst conduits (Sweeting, 1973; Ford and Williams, 2007). These processes eventually create unique karst landscapes at the large scale, but they invariably begin at the scale of individual pores.

The solubility of carbonate rocks depends on the pH of the water infiltrating it (Plummer and Wigley, 1976; Plummer et al., 1978; Sweeting, 1973). The sources of acidity include both the rainwater, which is in equilibrium with the atmospheric CO_2 as well as the biological activity in the soil. Both roots and soil bacteria produce relatively large quantities of carbon dioxide, dramatically increasing the pCO_2 of the infiltrating water. As a result, about 70 percent of the dissolution takes place in the top 10 m of limestone (Ford and Williams, 2007).

The mechanisms of limestone dissolution have been widely studied, mainly, however, through the laboratory experiments, often involving lower pH and thus faster reactions than natural dissolution. These experiments typically involve acidization of limestone cores with HCl or CO_2-saturated brine and observation of the resulting dissolution patterns (Hoefner and Fogler, 1988; Golfier et al., 2002; McDuff et al., 2010; Luquot et al., 2014).

Three different dissolution regimes emerge from these experiments, depending on the ratio of convective and reactive timescales in the system (Fredd and Fogler, 1998; Golfier et al., 2002; Ladd and Szymczak, 2021). If the reactant penetration length is much shorter than the system length, then dissolution is limited to the surface of the rock (face dissolution regime). In the other extreme, at high flow rates, when the penetration length is much longer than the system length, the sample dissolves uniformly, without any significant porosity gradients developing along the flow direction. Finally, for intermediate flow rates, the flow self-organizes in the dissolution channels (wormholes), which form a fractal network throughout the sample (Chadam et al., 1986; Hoefner and Fogler, 1988; Daccord, 1987; Szymczak and Ladd, 2014).

On the other hand, recent tomographic measurements provided insight into the dynamics of evolving pore space during chemical

* Corresponding author.
E-mail address: piotrek@fuw.edu.pl (P. Szymczak).

https://doi.org/10.1016/j.chemgeo.2023.121397
Received 13 September 2022; Received in revised form 28 December 2022; Accepted 22 February 2023
Available online 11 March 2023

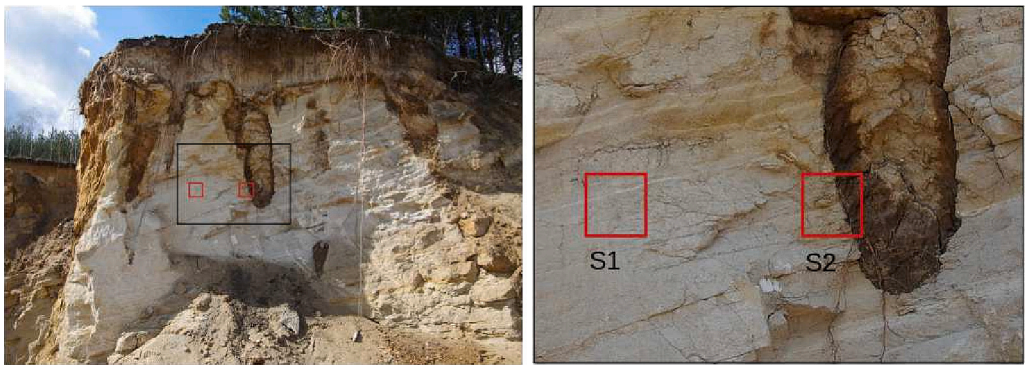

Fig. 1. Solution pipes in a Smerdyna quarry with locations of samples S1 and S2.

transformation (Noiriel et al., 2013; Luquot et al., 2014; Ott and Oedai, 2015; Garcia-Rios et al., 2015; Menke et al., 2016; Qajar and Arns, 2022b; Qajar and Arns, 2022a). Changes in the solid phase volume and the associated rock structure modifications characterized by changes in reactive surface area, tortuosity, or connectivity, have been assessed and linked with the reaction progress and the evolving flow paths in the sample. A proper quantification of these processes is crucial for building numerical models capable of predicting long-term changes in the properties of dissolving rocks. Such models can then be used for the prediction of sinkhole formation and ground subsidence in karst landscapes, or estimation of the effects of the long-lasting presence of large volumes of CO_2 in underground reservoirs, injected as a part of geologic carbon storage projects. And yet two characteristics of the dissolution make it notoriously hard to construct large-scale predictive models. The first element is the quantification of the changes in reactive surface area as a result of dissolution (Van Cappellen, 1996; Gautier et al., 2001; Noiriel et al., 2009; Luhmann et al., 2014). Understanding changes in reactive surface area is a key element of the attempts to upscale the description of the dissolution process from the pore-scale to the core- or reservoir scale (Luquot and Gouze, 2009; Noiriel et al., 2012; Bouissonnié et al., 2018; Poonoosamy et al., 2019; Yu et al., 2022). It is well-established that specific reactive surface area increases during the early stages of dissolution of rocks of relatively low initial porosity: the pores broaden, and a larger mineral surface becomes exposed. However, at a certain point, the trend reverses due to the pore merging, with reactive surface area eventually decreasing to zero as porosity approaches unity (Noiriel et al., 2009). Pore merging is arguably one of the most elusive processes in mineral dissolution, difficult to characterize in a quantitative manner (Schechter and Gidley, 1969). The second formidable aspect of dissolution is its multi-scale character: flow and transport are guided by large-scale characteristics of the medium, whereas chemical reactions are controlled by the local geometry of the fluid–mineral interface (Hoefner and Fogler, 1988; Li et al., 2007; Luquot and Gouze, 2009; Molins et al., 2014; Roded et al., 2021). This leads to the focusing of the dissolution in larger pore spaces where advection dominates the diffusion.

The present paper attempts to give insight into these problems, by analyzing changes in pore geometry in naturally dissolved limestone. In contrast to the large amount of data collected from lab dissolution experiments, there is only a handful of studies on changes in the pore geometry due to natural dissolution (Dubois et al., 2014; Merino and Banerjee, 2008). One of the reasons for such a situation might be the difficulty in making a comparison of the dissolved rock geometry with the original one, since, in many cases, the latter is no longer available, as the entire rock mass has undergone the transformation. Our samples are collected in a karstified area, where an intense flow focusing due to dissolution takes place, accompanied by the formation of solution pipes (Walsh and Morawiecka-Zacharz, 2001; Lipar et al., 2021) (Fig. 1). Due to spontaneous piping of the flow one infers that the rock immediately next to the pipe has been exposed to the aggressive flow, chemically eroding the rock matrix, whereas the rock masses in between the pipes remained unkarstified. This gives us an opportunity to characterize the changes in the pore geometry induced by natural dissolution.

The host rock is very porous (about 40% porosity) with irregular and highly interconnected pore spaces, which means that pore merging will play an important role in its evolution. At the same time, the lack of well-defined pore throats makes it difficult to apply standard tools of pore geometry analysis, such as the identification of individual pores and throats and the subsequent calculation of the pore size distribution. Such a geometry, lacking well-separated pore structures, needs to be characterized in a different manner. For this, we turned to the set of tools originally developed for bone research (Hildebrand and Rüegsegger, 1997; Dougherty and Kunzelmann, 2007), such as local thickness, ellipsoid factor, or connectivity. The combination of the tomographic data analysis with the simple analytical models allowed us to quantify the role of pore merging and inhomogeneous dissolution in the process of natural dissolution for the analyzed samples.

2. Materials and methods

2.1. Collection of samples

The research area is located near Smerdyna, Poland, about 12 km northeast of Staszow. Mining activities provide extensive exposures of mid-Miocene calcarenite with intense epikarst features. The calcarenites of the Chmielnik Formation around Smerdyna have an average carbonate content of more than 90% (Walsh and Morawiecka-Zacharz, 2001). The calcarenites are overlain by uncemented glacial till up to 5 m thick, from which the material filling solution pipes is derived (Morawiecka and Walsh, 1997; Walsh and Morawiecka-Zacharz, 2001).

Samples of Miocene calcarenites were collected from a fresh exposure in one of the quarries, where extensive epikarst development is observed on the open cut walls, mainly in the form of solution pipes that can reach a diameter of about 0.5 m and a length up to 6 meters (*cf.* Fig. 1). Sample S1 was extracted about 1.5 meters from the pipe, while sample S2 was collected directly from the side of a long and wide pipe. Both samples are cylindrical, 2.4 cm in length and 2.2 cm in diameter, taken perpendicular to the axis of the pipe. In the case of the sample S2, the top of the cylinder coincided with the surface of the pipe.

Visual inspection of sample S2 shows that it is considerably more porous and much softer than S1, at the edge of crumbling. This difference is confirmed by porosity measurement (following the hydrostatic method ISO 5017), which gives the porosity of S1 at $\varphi_1 = 39.35 \pm 0.8\%$ whereas that for S2 is $\varphi_2 = 50.7 \pm 0.6\%$. This porosity difference most likely corresponds to the dissolution of the sample S2 by CO_2 -saturated water, which was focused in the pipe. Therefore, we have the opportunity to observe the differences between the naturally dissolved samples (S2) and relatively undissolved (S1) samples originating from the same host rock.

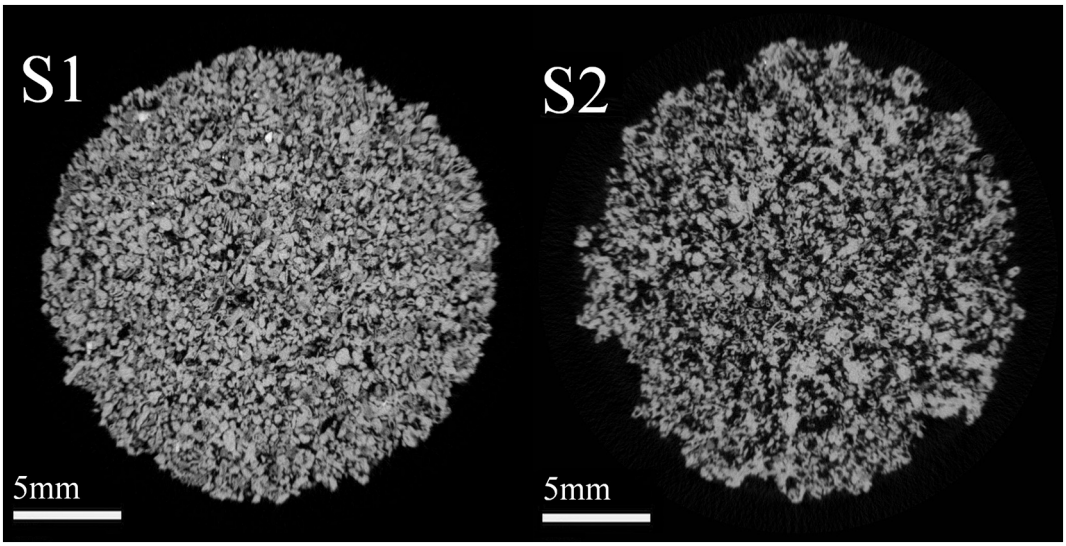

Fig. 2. The tomographic images of the undissolved sample (S1, left) and naturally dissolved sample (S2, right).

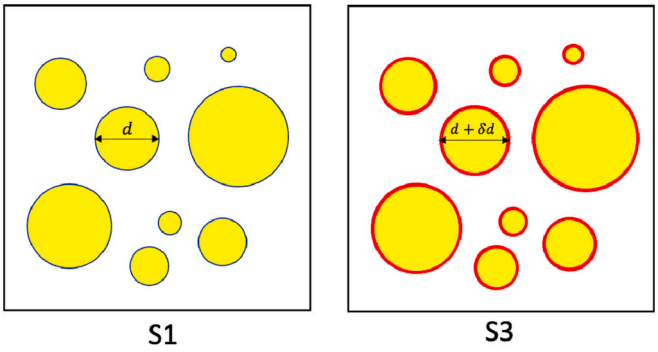

Fig. 3. Numerical erosion of the samples: starting from the undissolved sample (S1, with pores depicted in yellow and rock matrix - in white) we produce a homogeneously dissolved one (S3) by removing a fraction of the voxels at pore-grain boundaries (marked in red in the figure) and smoothing it using median filter.

2.2. X-ray microtomography

Samples were scanned using an Xradia MicroXCT-200 X-ray imaging system at the Institute of Paleobiology, Polish Academy of Sciences. These scans consist of 648, 1024×1024 16-bit grayscale slices with a voxel resolution of 26 μm.

The obtained X-ray microtomography scans were studied using ImageJ image processing software (Schneider et al., 2012). Fig. 2 shows a single slice of a tomographic image for both samples. To simplify the comparison between the samples, a cubical region of interest (ROI) was chosen in each sample. The size of each region is 506^3 voxels, corresponding to $(13.2\text{mm})^3$. Additionally, these image stacks were converted to 8-bit images to reduce the size of the data for computational purposes. Finally, the images were segmented by tuning the grayscale threshold to match the experimentally measured porosity values of the respective samples. The porosity variation within both cores is relatively small (within 3%) with no macroscopic porosity gradients observed. The general appearance of the scans (as shown in Fig. 2) confirms a much rougher appearance of the naturally dissolved sample, S2. However, our goal here is to characterize these differences in a more quantitative manner in order to learn something about the dissolution process itself.

2.3. Numerically eroded sample

To understand which features of the natural dissolution are similar to homogeneous dissolution and which are different we have numerically generated another pore geometry. Starting from the segmented geometry of the undissolved sample, S1, we randomly removed the voxels at grain/pore boundary with probability p tuned so as to guarantee that the total porosity increase is equal to 11.35%, i.e., exactly matching the porosity difference between samples S1 and S2. After numerical erosion we smoothed out the boundaries between the grains and the pores using a median filter with the radius of one voxel. Since each boundary voxel has the same probability of being removed, such a procedure mimics a fully homogeneous dissolution of the rock. In the following, we will refer to the geometry created in such a manner as S3 (see Fig. 3). Note that, by

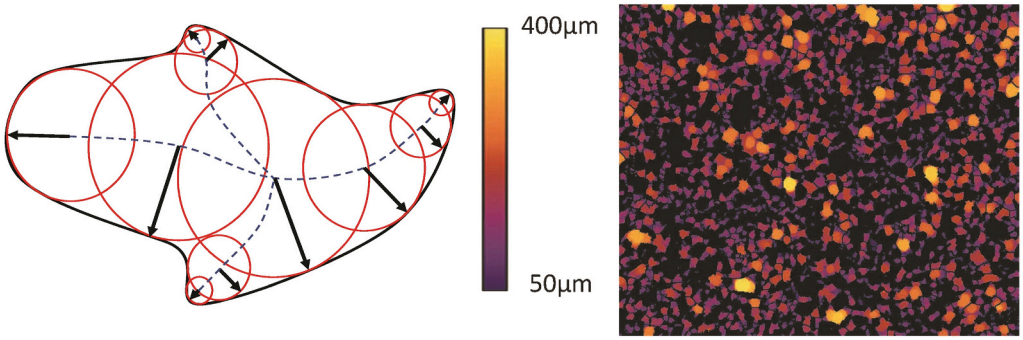

Fig. 4. Left: Schematic illustration of a local thickness measurement. Right: local thickness map of a cross-section of sample S1.

construction, the porosities of S2 and S3 coincide. Additionally, for consistency, we have applied the identical median filter to the original geometries of both S1 and S2.

2.4. Pore space characterization

Irregular geometry of the pore space, the vast majority of which forms a single connected component, lacking well-defined pore bodies and throats makes it difficult to apply standard tools of pore space analysis such as the identification of individual pores and the subsequent calculation of the pore size distribution. The division of the pore space into individual pores becomes then somewhat arbitrary, to a large extent dependent on the parameters used in the pore-segmentation algorithm (e.g. watershedding) (Sheppard et al., 2005). In such cases, it might be advantageous to use continuous measures of the pore (and grain) space, such as the local thickness or ellipsoid factor (Hildebrand and Rüegsegger, 1997; Dougherty and Kunzelmann, 2007), which are defined in each point of the sample. However, a standard pore network extraction algorithm, identifying pore bodies and throats is a viable alternative for samples of smaller porosity, particularly when combined with mercury intrusion porosimetry (Menke et al., 2015; Qajar and Arns, 2022b).

2.4.1. Local thickness

The most important measure to characterize such an interconnected pore space is the local thickness. Defined locally at each point, local thickness is the diameter of the largest sphere to which a given point belongs and which fits within the pore, as illustrated in Fig. 4 (Hildebrand and Rüegsegger, 1997; Dougherty and Kunzelmann, 2007). Note that the local thickness of the pore space defined in such a way is different from both the pore diameter or pore throat size and gives an independent measure of the pore extent. The term "thickness" can be somewhat misleading in a petrological context, where it is usually associated with the extent of rock strata, but it has a wide use in 3D microscopic measuring techniques and image analysis (Hildebrand and Rüegsegger, 1997; Dougherty and Kunzelmann, 2007) for characterization of extended 3D structures.

In the context of digital rock physics, local thickness has been used to characterize the pore-scale configurations of fluids in a multiphase flow problems (Scanziani et al., 2018; Scanziani et al., 2020), to characterize constrictions in the pore space for interpretation of mercury intrusion porosimetry experiments (Louis, 2019), and - what is most relevant in the present context - to quantify the opening of the pore spaces during the dissolution experiments (Voltolini and Ajo-Franklin, 2019).

In this work, the local thickness (as well as other measures detailed below) are calculated with the help of the BoneJ plugin for ImageJ (Doube et al., 2010), originally developed for trabecular bone analysis. In fact, the trabecular bone pore space shares a lot of characteristics with the extended and irregular pore space of the analyzed rock samples. Importantly, local thickness can also be defined for a grain phase, in a fully analogous manner to the thickness of the pore space, by looking for the largest sphere that fits in the grain phase only and contains the point of the measurement.

2.4.2. Ellipsoid factor and Flinn diagram

Characterization of the pore space/matrix by local thickness can be further extended by assigning more information related to the geometry of the surrounding space to a point of interest. This is achieved by fitting locally not a sphere, but a maximum ellipsoid (see Doube (2015) for a detailed description). For an ellipsoid with axes $A \leqslant B \leqslant C$, the ellipsoid factor EF is then defined as the difference of axes ratios

$$EF = \frac{A}{B} - \frac{B}{C},$$

which differentiate between oblate (pancake-like) shapes (for $A/B \to 0$ and $B/C \to 1$) and prolate (cigar-like) shapes (for $A/B \to 1$ and $B/C \to 0$). For illustration purposes, we use the Flinn diagram (Flinn, 1962; Doube, 2015), which is a 2d plot in the coordinates of A/B versus B/C.

2.4.3. Connectivity

Connectivity (β_1) is a measure of the degree to which a structure is interconnected. Quantitatively, for a graph (or network), it corresponds to the maximal number of edges (links) that can be removed while leaving the structure connected, i.e. not separated into disjoint parts (Odgaard and Gundersen, 1993). It is a topological invariant of the pore space, hence it is preserved under deformations as long as they do not involve cutting of the grains or filling the holes. Another, more widely known topological invariant is the Euler characteristic χ, related to connectivity by the Euler-Poincare formula, which for 3D geometry reads

$$\chi = \beta_0 - \beta_1 + \beta_2,$$

where β_0 and β_2 are the so-called zeroth and second Betti numbers (Janich, 1984) (the first Betti number, β_1 is the connectivity itself). In our context (rock matrix), β_0 can be interpreted as the number of connected pieces (components) of the rock, which is normally equal to unity. On the other hand, β_2 corresponds to the number of cavities in the rock (Odgaard and Gundersen, 1993), which can be greater than 0 if there is closed porosity in the sample.

BoneJ calculates connectivity by relating it to these Euler characteristics. To do so, it first *purifies* the sample, imposing $\beta_2 = 0$, which is equivalent to filling all closed pores.

2.5. Permeability, tortuosity and velocity distribution

We supplement the analysis of the geometrical characteristics of the pore space by a numerical computation of flow field through the ROI of our samples. We solve the Stokes equations in the pore space obtained directly from the segemented tomographic images, using the lattice-Boltzmann method implemented with the Palabos library (Weller et al., 1998). The absolute permeability of the sample is then obtained by integrating the flow velocity through the cross-section, whereas the tortuosity can be estimated as (Duda et al., 2011)

$$\tau = \frac{\langle u \rangle}{\langle u_x \rangle}, \tag{1}$$

where $\langle u \rangle$ is the average magnitude of the Darcy velocity over the entire system volume and $\langle u_x \rangle$ is the volumetric average of its component along the macroscopic flow direction. Finally, we also analyze the distributions of velocities for both samples and compare them.

3. Results and discussion

Using the above methods, we study the pore space geometry by comparing the ROI of real samples S1 and S2, and the numerically eroded sample S3, used here as a reference to homogeneous dissolution.

As mentioned, even before dissolution, the samples are highly porous (~40% primary porosity), with a highly irregular, complex pore structure. Furthermore, the reactive surface area is also high. A direct count of the voxel sides constituting pore-matrix boundaries in the segmented image leads to an estimate of a specific reactive surface area $s_1 \approx 10.0 \mathrm{mm}^2/\mathrm{mm}^3$, comparable to, or larger than, other limestones of similar porosity (Noiriel et al., 2009). For a sample of such high porosity and reactive surface area, dissolution, even uniform, may result in significant changes in the topology of the pore space, as some walls between pores will be completely dissolved. Hence, we anticipate that merging between the pores might be an important process in Smerdyna Limestone. Indeed, the dissolved rock sample has a specific reactive surface area $s_2 \approx 9.1 \mathrm{mm}^2/\mathrm{mm}^3$, i.e. about 10% smaller than s_1. The decrease of s in the course of dissolution shows that pore merging plays an important role in the dissolution process. This makes it

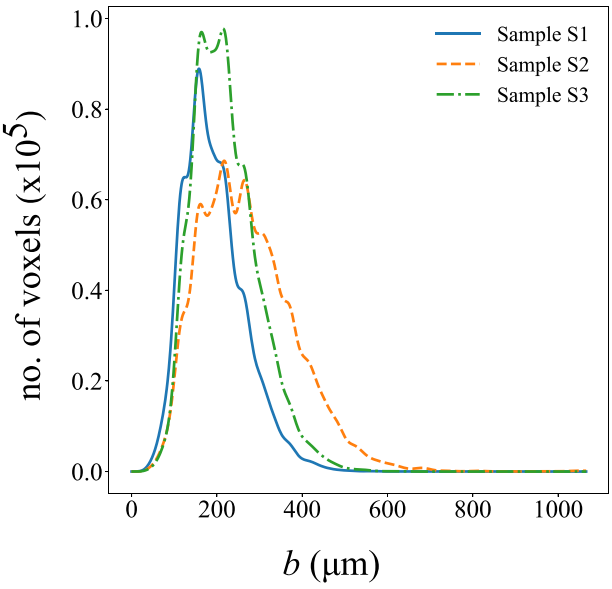

Fig. 5. Local thickness distribution for samples S1, S2 and S3. The counts correspond to the number of voxels with local thickness in the range $(b-\frac{\Delta b}{2}, b+\frac{\Delta b}{2})$ with the bin size $\Delta b = 0.26$ μm.

fundamentally different from the dissolution of packed limestones, which is dominated by the dilation of the pores, without merging.

Fig. 5 presents local thickness distribution for samples S1, S2 and S3, describing the number of voxels characterized by a given local thickness. The distribution is obtained using the BoneJ plugin of ImageJ and then processed using a local-Gaussian filter for smoothing out the curves, i.e. removal of artificially variability in data resulting from the voxelization effects in small pores.

As observed, for small local thicknesses (below 100 μm), the distributions of S2 and S3 overlap. When interpreting these data, we should bear in mind that S3 has been obtained from S1 by fully uniform dissolution, removing a layer of equal thickness throughout the rock matrix. From the overlap of the local thickness distributions, $P(b)$, for small b, we thus conclude that, in the process of natural dissolution, the smallest pores increase in size in an approximately uniform manner. On the other hand, the large-thickness tail of the distribution $P(b)$ for the dissolved sample S2 is much higher, not only in relation to the undissolved sample S1, but also with respect to the uniformly eroded sample S3. This shows that most of the dissolution has been focused in the largest pore spaces.

As mentioned above, no macro-scale porosity gradients were observed in the dissolved sample, leading us to the conclusion that the reactant penetration length was much larger than the sample size. This is the so-called uniform dissolution regime (Golfier et al., 2002; Hoefner and Fogler, 1988; Szymczak and Ladd, 2009; Menke et al., 2016; Cohen et al., 2008), in the sense that dissolution occurs throughout the rock matrix and not only near the inlet of a reactive fluid. However, if the dissolution was truly uniform across the pore space, then the statistical properties of the naturally dissolved sample (S2) should resemble those of a numerically dissolved one (S3). This is clearly not the case, with the largest pores spaces being preferentially dissolved.

Note that this effect (of relatively higher dissolution of larger pore structures) is not connected to the phenomenon of pore-controlled solubility (Lifshitz and Slyozov, 1961; Emmanuel et al., 2010). Indeed, the interphase surface tension results in a solubility dependence on the pore size

$$c(r) = c_\infty e^{2\nu\gamma/(N_A k_B T r)}$$

where r is the pore size, γ is interfacial energy, T is the temperature, N_A is the Avogadro number, ν is the molar volume of the mineral, and c_∞ is the bulk solubility. However, for calcite, interfacial energy contributes appreciably to the solubility only for pores below 1 μm (Emmanuel and Berkowitz, 2007), i.e., much below the range of sizes considered in the present study.

Table 1
Characteristics of the local thickness distribution of the samples S1–S3.

local thickness (μm)	S1	S2	S3
pores (max)	588 ± 52	1097 ± 159	641 ± 43
pores (mean)	184 ± 8	261 ± 15	221 ± 9
pores (std)	68 ± 3	109 ± 12	75 ± 3
grains (max)	840 ± 48	764 ± 51	807 ± 43
grains (mean)	245 ± 5	262 ± 7	226 ± 4
grains (std)	90 ± 4	104 ± 4	87 ± 4

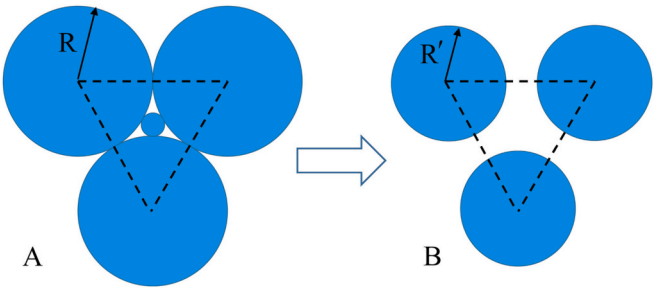

Fig. 6. A simple conceptual model showing the asymmetry between growth of pore thickness and decrease of grain thickness: initial geometry (A) and the geometry after the dissolution (B). As shown in the Appendix, the pore thickness in this process increases by approx. $0.49R$ whereas the grain thickness decreases by about $0.23R$ only.

Instead, we link our observations to the experimental findings of Menke et al. (2016), who conducted a series of experiments on the dissolution of limestones by CO_2-saturated brine in the uniform dissolution regime. They found that the heterogeneity of the rock allows preferential flow paths to form under such conditions, transporting the majority of the reactant to a relatively limited portion of the surface of the rock. Since the permeability of the pore structures strongly increases with the pore size (as quantified by the local thickness), we expect the preferential pathways to involve mostly the high-thickness regions, which should result in the most intense growth of such pore spaces, as indeed observed in Fig. 5. A similar effect was also observed in the experimental studies of Egermann et al. (2010) and Qajar and Arns (2022b), who analyzed experimentally limestone dissolution in a uniform regime and observed the preferential growth of larger pores.

Further insight into the nature of natural dissolution can be obtained from the analysis of distribution statistics, as shown in Table 1. Before we discuss these results, let us first note that - in the process of dissolution - local thickness of the pore space can increase due to two different mechanisms. The first is the growth of individual pores and the second is merging between them. If the pores were simply growing, without merging, then the thickness would increase on average,

$$\Delta b \approx 2(\varphi_2 - \varphi_1)/s_1 = 22.7\ \mu\text{m}.$$

This is a much smaller increase than the local thickness difference between the numerically eroded sample S3 and the undissolved S1, which is approximately 34 μm. This suggests that merging is an important mechanism in the local thickness increase, which is fully consistent with the high porosity of the original sample. However, the increase in local thickness in the naturally dissolved sample S2 with respect to S1 is even greater, more than 70 μm. This again suggests that the dissolution is nonuniform and focuses in spaces of the largest local thickness. The contribution of these regions to the average is dominant (scaling as b^3);

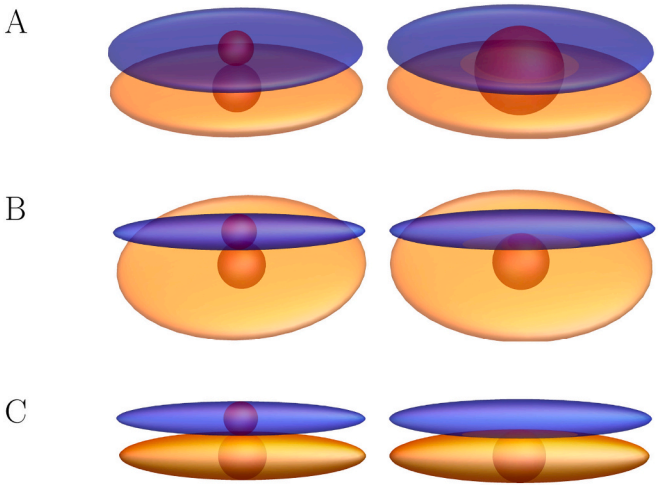

Fig. 7. Merging of two oblate spheroidal pores (A), an oblate and prolate pore (B), and two prolate spheroidal pores (C). The left column shows the pores just before merging, in the right column the pores are enlarged by dissolution and they intersect. Red balls correspond to the maximal inscribed spheres inside the pores. In (C) the increase of local thickness is only due to the dissolution, with no contribution from merging. In (B) there is a relatively small, but nonzero, increase in b due to merging. Finally, in (A) there is a significant increase of local thickness, most of it due to merging.

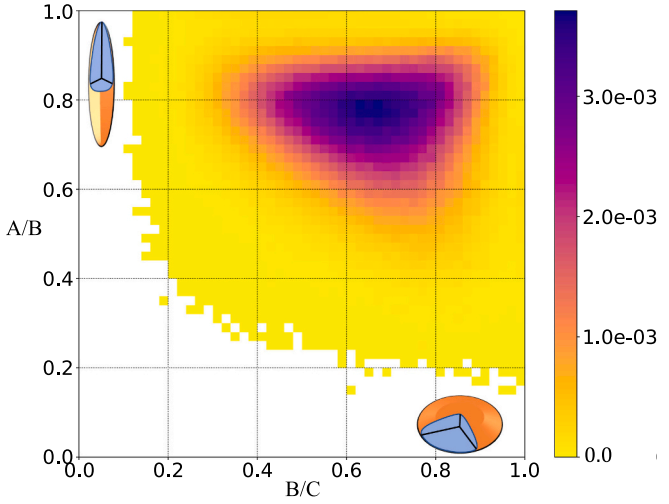

Fig. 8. Flinn diagram for the undissolved sample. The colors indicate value of the contribution to the total pore volume coming from specific shape - i.e. volumes for which the largest inscribed ellipsoid has values of A/B and B/C from specific ranges. All contributions sum to 1. Oblate shapes correspond to small A/B and relatively large B/C.

therefore, any additional increase in their local thickness results in a dramatic growth of $< b >$.

Another intriguing observation based on the data in Table 1 is that while the average thickness of the pore space is significantly larger in the dissolved sample with respect to the undissolved one, the average thickness of the rock phase (grains) is approximately the same. Naively, one would expect these two effects to balance each other, with the thickness of grains decreasing by approximately the same amount as the thickness of pore increased. This would indeed be the case if the pores in the sample were well-separated. However, as we argue below, merging of the pores disrupts this balance. To illustrate it, we consider a simple two-dimensional pore geometry, shown in Fig. 6. In this conceptual model, we consider a small grain surrounded by a number of larger

Table 2
Connectivity (χ) for samples S1–S3.

	S1	S2	S3
χ	139987	82438	103955

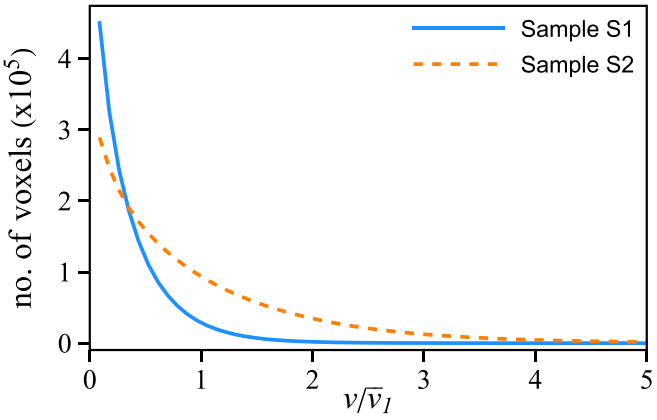

Fig. 9. The distribution of velocities in the dissolved and undissolved sample. The velocities are normalized by the mean velocity in the undissolved sample. The bin size used to calculate the counts is $\Delta = 0.004$.

grains and pore spaces, which, after dissolution, merge together. As shown in the Appendix, as a result of the merging of the pores, the increase of the pore thickness is more than twice the decrease of the grain thickness.

Moving to three spatial dimensions, let us observe that not all of the pore shapes increase their average thickness considerably while merging. The largest relative increase is expected for oblate, pancake-like shapes. Their initial thickness is approximately equal to their depth (as illustrated in Fig. 7) and can increase significantly when two such pores merge. On the other hand, if merging takes place between two prolate, cigar-like ellipsoids, then their thickness increases only slightly.

As a consequence, if we claim that local thickness increases as a result of the pore merging, we should also ascertain that at least some of the pores are of the oblate shape, since the merging between two prolate shapes or even the prolate and oblate shape results in a relatively modest increase of the local thickness. This information can be read off the corresponding Flinn diagram for an undissolved sample, as presented in Fig. 8. The diagram shows the fraction of the pore volume for which the largest inscribed ellipsoid has specific values of A/B and B/C (as marked on the axes). Oblate shapes correspond to relatively small A/B and relatively large B/C. Although most of the pore shapes are neither oblate nor prolate, there is in fact a considerable fraction of oblate pores in our sample.

The evolution of the pore structure during natural dissolution is also reflected in the change in connectivity, χ, as shown in Table 2. The change of connectivity during dissolution is a direct measure of merging in the sample, since χ - as a topological invariant - does not change as the pores increase their radius if merging is not involved. As observed, χ strongly decreases as a result of the dissolution: there is a 25% decrease in connectivity between S1 and S3 due to the merging related to the uniform dissolution of the pore space. However, the connectivity of the naturally dissolved sample, S2, is reduced by an additional 20%, indicating extra merging due to focusing of the dissolution in the largest pore spaces.

Finally, the changed topology of the pore space is also reflected in the flow characteristics, which we calculate as described in Section 2.5. The dissolved sample has a larger overall permeability than an undissolved one, with the ratio $K_2/K_1 \approx 4.15$. This is more than expected from a simple application of Kozeny–Carman equation, $K(\varphi) \sim \varphi^3/(1-\varphi)^2$

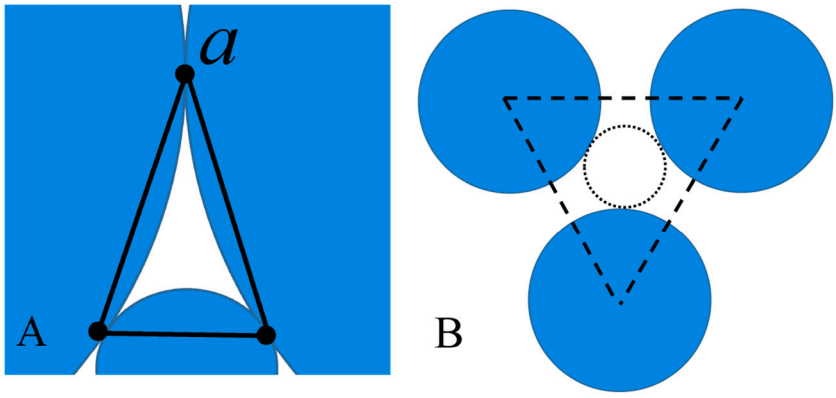

Fig. 10. (A) A portion of the initial pore space in the model of Fig. 6. (B) The final pore space with a central circle of radius 2r (dotted).

which would give $K_2/K_1 \approx 3.24$, which indicates an extra flow focusing in larger pores. The tortuosity of the undissolved sample, calculated based on Eq. (1) was equal to $\tau_1 = 1.463$ whereas the tortuosity of the dissolved sample were calculated to be $\tau_2 = 1.323$. The straightening of flow paths associated with a decrease of tortuosity during dissolution is fully consistent with the results for experimentally dissolved samples (Pereira Nunes et al., 2016; Luquot et al., 2014). Interestingly, as noted by Luquot et al. (2014) the appreciable (> 10%) tortuosity decrease is observed usually in the uniform dissolution regime, whereas in the wormhole formation regime the changes of tortuosity are relatively small.

The emergence of faster flowing regions in the sample is further confirmed by the analysis of the velocity distribution (Fig. 9), which shows a distinct shift towards the larger values with an emergence of fat tail at the larger velocity values.

4. Conclusions

In this study, we have investigated the changes of pore space geometry incurred in natural samples as a result of dissolution. The small porosity gradients observed in a dissolved sample led us to the conclusion that dissolution proceeded in a uniform regime, with a reactant penetration length much larger than the system size. Naively, one would expect that uniform dissolution should result in the removal of a constant layer of mineral from all the rock surfaces and the associated increase in the local thickness by $\Delta b = 2\Delta\varphi/s$, however, the actual increase in local thickness is much larger. One important mechanism is merging of the pores, which is prevalent in a sample of such high porosity. Merging can significantly increase the local thickness of the pore space; in the extreme case (if the merging pores are oblate in shape), the merged pore will have a thickness equal to the sum of the thicknesses of the constituents. However, it turns out that merging itself cannot explain all of the changes in the pore-space geometry. We observe strong focusing of dissolution in the largest pore spaces, which can be described in terms of the uniform channeling regime, with the emergence of preferential pathways linking the regions of the highest local permeability. This is also reflected in the decrease of tortuosity of the flow paths, and the increase of the fraction of the faster flow in the sample.

From a more general perspective, a set of tools presented in this paper should allow one to delineate the effects of uniform dissolution of individual pores, merging and emergence of preferential flow paths during dissolution, both in natural and laboratory settings.

Declaration of Competing Interest

The authors declare that they have no known competing financial interests or personal relationships that could have appeared to influence the work reported in this paper.

Data availability

Data will be made available on request.

Acknowledgments

RPS, MPC, APR, and PS have been supported by the National Science Center (Poland) under research Grant No. 2016/21/B/ST3/01373. MB has been supported by a subsidy from the Polish Ministry of Education and Science for the Institute of Geophysics, Polish Academy of Sciences and by the National Science Center (Poland) under research Grant No. 2017/27/B/ST10/02686.

Appendix

Here, we present an analytical estimate of the asymmetry between the increase in pore thickness and the decrease in grain thickness in the simple 2D model presented in Fig. 6. The initial geometry of the model involves three grains represented by disks in the figure, all with the same radius (R), tangent to each other. There is also a smaller grain of radius r, tangent to all three larger grains, with $r = (\frac{2\sqrt{3}}{3} - 1)R \approx 0.155R$. Let us now assume that such a setup dissolves uniformly, until the central grain vanishes. At this point, the radii of the larger grains become $R' = R - r$ as shown in Fig. 6. The average thickness of the grain phase in the initial configuration is then

$$b^i_{grain} = \frac{2R\cdot\frac{1}{2}\pi R^2 + 2r\cdot\pi r^2}{\frac{1}{2}\pi R^2 + \pi r^2} \approx 1.92R,$$

where the average was taken over the triangular cell marked with dashed lines in Fig. 6.

In the final configuration, the central grain has fully dissolved, whereas the three large grains have shrunk to $R' = R - r$. The average thickness for the final state is thus

$$b^f_{grain} = 2(R - r) \approx 1.69R,$$

and the change in thickness as a result of dissolution is

$$b^f_{grain} - b^i_{grain} \approx -0.23R.$$

To estimate the average thickness of the pores, we note that the pore space consists of three curvilinear triangles in between the grains. Approximating each one of these by a triangle (as shown in Fig. 10) we note, from the elementary geometrical considerations, that the radius of a maximal circle inscribed in such a pore space is

$$y = r\cdot\frac{\frac{R}{\sqrt{3}} - r}{\frac{R}{\sqrt{3}} + r} \approx 0.089R.$$

This is a maximum thickness attainable in this triangle; however, points closer to the vertex a will have a progressively smaller thickness, decreasing linearly with the distance to a. The average thickness can then be approximated as

$$b^i_{pore} \approx \frac{\int_0^y x^2 dx}{\int_0^y x dx} = \frac{2}{3}y \approx 0.06R.$$

Finally, we estimate the average thickness in the final state after dissolution. The pore space within the dashed triangle in Fig. 10B can be divided into two parts: the central circle of diameter $2r$ (dotted in the Figure) and the side areas between the disks in which the thickness changes between $\approx 2r$ and $4r$. The area of this region is

$$S = \sqrt{3}R^2 - \frac{1}{2}\pi(R - r)^2 - \pi(2r)^2,$$

and the average thickness in this region is again approximated by the integral

$$\frac{\int_{2r}^{4r} x^2 dx}{\int_{2r}^{4r} x dx} = \frac{28}{9}r.$$

Hence,

$$b^f_{pore} \approx \frac{4r\cdot 4\pi r^2 + \frac{28}{9}r\cdot S}{4\pi r^2 + S} \approx 0.55R,$$

and the change of thickness as a result of dissolution is

$$b^f_{pore} - b^i_{pore} \approx 0.49R,$$

more than twice larger than the corresponding decrease in the grain thickness.

References

Bouissonnié, A., Daval, D., Marinoni, M., Ackerer, P., 2018. From mixed flow reactor to column experiments and modeling: Upscaling of calcite dissolution rate. Chem. Geol. 487, 63–75.

Chadam, D., Hoff, D., Merino, E., Ortoleva, P., Sen, A., 1986. Reactive infiltration instabilities. J. Appl. Math. 36, 207–221.

Cohen, C., Ding, D., Quintard, M., Bazin, B., 2008. From pore scale to wellbore scale: Impact of geometry on wormhole growth in carbonate acidization. Chem. Eng. Sci. 63, 3088–3099.

Daccord, G., 1987. Chemical dissolution of a porous medium by a reactive fluid. Phys. Rev. Lett. 58 (5), 479–482.

Doube, M., 2015. The ellipsoid factor for quantification of rods, plates, and intermediate forms in 3D geometries. Front. Endocrinol. 6, 15.

Doube, M., Kłosowski, M.M., Arganda-Carreras, I., Cordelières, F.P., Dougherty, R.P., Jackson, J.S., Schmid, B., Hutchinson, J.R., Shefelbine, S.J., 2010. BoneJ: free and extensible bone image analysis in ImageJ. Bone 47 (6), 1076–1079.

Dougherty, R., Kunzelmann, K.-H., 2007. Computing local thickness of 3D structures with ImageJ. Microsc. Microanal. 13 (S02), 1678–1679.

Dubois, C., Quinif, Y., Baele, J.-M., Barriquand, L., Bini, A., Bruxelles, L., Dandurand, G., Havron, C., Kaufmann, O., Lans, B., et al., 2014. The process of ghost-rock karstification and its role in the formation of cave systems. Earth Sci. Rev. 131, 116–148.

Duda, A., Koza, Z., Matyka, M., 2011. Hydraulic tortuosity in arbitrary porous media flow. Phys. Rev. E 84 (3), 036319.

Egermann, P., Bekri, S., Vizika, O., 2010. An integrated approach to assess the petrophysical properties of rocks altered by rock-fluid interactions (CO2 Injection). Petrophysics 51, 32–40.

Emmanuel, S., Ague, J.J., Walderhaug, O., 2010. Interfacial energy effects and the evolution of pore size distributions during quartz precipitation in sandstone. Geochim. Cosmochim. Acta 74 (12), 3539–3552.

Emmanuel, S., Berkowitz, B., 2007. Effects of pore-size controlled solubility on reactive transport in heterogeneous rock. Geophys. Res. Lett. 34, L06404.

Flinn, D., 1962. On folding during three-dimensional progressive deformation. Quart. J. Geol. Soc. 118 (1–4), 385–428.

Ford, D.C., Williams, P., 2007. Karst Hydrogeology and Geomorphology. Wiley, Chichester, UK.

Fredd, C.N., Fogler, H.S., 1998. Influence of transport and reaction on wormhole formation in porous media. AIChE J. 44, 1933–1949.

Garcia-Rios, M., Luquot, L., Soler, J.M., Cama, J., 2015. Influence of the flow rate on dissolution and precipitation features during percolation of CO_2-rich sulfate solutions through fractured limestone samples. Chem. Geol. 414, 95–108.

Gautier, J.-M., Oelkers, E.H., Schott, J., 2001. Are quartz dissolution rates proportional to B.E.T. surface areas? Geochim. Cosmochim. Acta 65 (7), 1059–1070.

Golfier, F., Zarcone, C., Bazin, B., Lenormand, R., Lasseux, D., Quintard, M., 2002. On the ability of a Darcy-scale model to capture wormhole formation during the dissolution of a porous medium. J. Fluid Mech. 457, 213–254.

Hildebrand, T., Rüegsegger, P., 1997. A new method for the model-independent assessment of thickness in three-dimensional images. J. Microsc. 185 (1), 67–75.

Hoefner, M.L., Fogler, H.S., 1988. Pore evolution and channel formation during flow and reaction in porous media. AIChE J. 34, 45–54.

Janich, K., 1984. Topology. Springer Verlag.

Ladd, A.J., Szymczak, P., 2021. Reactive flows in porous media: Challenges in theoretical and numerical methods. Annu. Rev. Chem. Biomol. Eng. 12, 543–571.

Li, L., Peters, C.A., Celia, M.A., 2007. Effects of mineral spatial distributions on reaction rates in porous media. Water Resour. Res. 43, W01419.

Lifshitz, I.M., Slyozov, V.V., 1961. The kinetics of precipitation from supersaturated solid solutions. J. Phys. Chem. Solids 19 (1–2), 35–50.

Lipar, M., Szymczak, P., White, S.Q., Webb, J.A., 2021. Solution pipes and focused vertical water flow: Geomorphology and modelling. Earth-Sci. Rev. 218, 103635.
Louis, L., 2019. Strength model parameterization as a building block for image-based prediction of mechanical properties. In: 53rd US Rock Mechanics/Geomechanics Symposium. pp. 19–0015.
Luhmann, A.J., Kong, X.-Z., Tutolo, B.M., Garapati, N., Bagley, B.C., Saar, M.O., Seyfried Jr, W.E., 2014. Experimental dissolution of dolomite by CO2-charged brine at 100C and 150 bar: Evolution of porosity, permeability, and reactive surface area. Chem. Geol. 380, 145–160.
Luquot, L., Gouze, P., 2009. Experimental determination of porosity and permeability changes induced by injection of CO_2 into carbonate rocks. Chem. Geol. 265 (1–2), 148–159.
Luquot, L., Rodriguez, O., Gouze, P., 2014. Experimental characterization of porosity structure and transport property changes in limestone undergoing different dissolution regimes. Transp. Porous Media 101 (3), 507–532.
McDuff, D.R., Shuchart, C.E., Jackson, S.K., Postl, D., Brown, J.S., 2010. Understanding wormholes in carbonates: Unprecedented experimental scale and 3-D visualization. J. Petrol. Technol. 62, 78–81.
Menke, H., Andrew, M., Blunt, M., Bijeljic, B., 2016. Reservoir condition imaging of reactive transport in heterogeneous carbonates using fast synchrotron tomography—Effect of initial pore structure and flow conditions. Chem. Geol. 428, 15–26.
Menke, H.P., Bijeljic, B., Andrew, M.G., Blunt, M.J., 2015. Dynamic three-dimensional pore-scale imaging of reaction in a carbonate at reservoir conditions. Environ. Sci. Technol. 49 (7), 4407–4414.
Merino, E., Banerjee, A., 2008. Terra Rossa genesis, implications for Karst, and Eolian dust: A geodynamic thread. J. Geol. 116, 62–75.
Molins, S., Trebotich, D., Yang, L., Ajo-Franklin, J.B., Ligocki, T.J., Shen, C., Steefel, C.I., 2014. Pore-scale controls on calcite dissolution rates from flow-through laboratory and numerical experiments. Environ. Sci. Technol. 48 (13), 7453–7460.
Morawiecka, I., Walsh, P., 1997. A study of solution pipes preserved in the Miocene limestones (Staszów, Poland). Acta Carsologica 20, 337–350.
Noiriel, C., Gouze, P., Made, B., 2013. 3D analysis of geometry and flow changes in a limestone fracture during dissolution. J. Hydrol. 486, 211–223.
Noiriel, C., Luquot, L., Madé, B., Raimbault, L., Gouze, P., van der Lee, J., 2009. Changes in reactive surface area during limestone dissolution: An experimental and modelling study. Chem. Geol. 265, 160–170.
Noiriel, C., Steefel, C.I., Yang, L., Ajo-Franklin, J., 2012. Upscaling calcium carbonate precipitation rates from pore to continuum scale. Chem. Geol. 318, 60–74.
Odgaard, A., Gundersen, H., 1993. Quantification of connectivity in cancellous bone, with special emphasis on 3-D reconstructions. Bone 14 (2), 173–182.
Ott, H., Oedai, S., 2015. Wormhole formation and compact dissolution in single-and two-phase CO_2-brine injections. Geophys. Res. Lett. 42, 2270–2276.
Pereira Nunes, J., Blunt, M., Bijeljic, B., 2016. Pore-scale simulation of carbonate dissolution in micro-CT images. J. Geophys. Res. Solid Earth 121 (2), 558–576.
Plummer, L.N., Wigley, T.L.M., 1976. The kinetics of calcite dissolution in CO2-water systems at 25C and 1 atmosphere total pressure. Geochim. Cosmochim. Acta 40, 191–202.
Plummer, L.N., Wigley, T.L.M., Parkhurst, D.L., 1978. The kinetics of calcite dissolution in CO2-water systems at 5C to 60C and 0.0 to 1.0 atm of CO2. Am. J. Sci. 278, 179–216.
Poonoosamy, J., Westerwalbesloh, C., Deissmann, G., Mahrous, M., Curti, E., Churakov, S.V., Klinkenberg, M., Kohlheyer, D., von Lieres, E., Bosbach, D., et al., 2019. A microfluidic experiment and pore scale modelling diagnostics for assessing mineral precipitation and dissolution in confined spaces. Chem. Geol. 528, 119264.
Qajar, J., Arns, C.H., 2022a. Chemically induced evolution of morphological and connectivity characteristics of pore space of complex carbonate rock via digital core analysis. Water Resour. Res. 58 (3), e2021WR031298.
Qajar, J., Arns, C.H., 2022b. A comparative study of micro-CT and mercury intrusion techniques for predicting permeability and surface area evolution during chemical dissolution. Adv. Water Res. 168, 104301.
Roded, R., Szymczak, P., Holtzman, R., 2021. Wormholing in anisotropic media: Pore-scale effect on large-scale patterns. Geophys. Res. Lett. 48 (11), e2021GL093659.
Scanziani, A., Singh, K., Bultreys, T., Bijeljic, B., Blunt, M.J., 2018. In situ characterization of immiscible three-phase flow at the pore scale for a water-wet carbonate rock. Adv. Water Res. 121, 446–455.
Scanziani, A., Singh, K., Menke, H., Bijeljic, B., Blunt, M.J., 2020. Dynamics of enhanced gas trapping applied to CO_2 storage in the presence of oil using synchrotron X-ray micro tomography. Appl. Energy 259, 114136.
Schechter, R., Gidley, J., 1969. The change in pore size distribution from surface reactions in porous media. AIChE J. 15 (3), 339–350.
Schneider, C.A., Rasband, W.S., Eliceiri, K.W., 2012. NIH Image to ImageJ: 25 years of image analysis. Nat. Methods 9 (7), 671–675.
Sheppard, A., Sok, R., Averdunk, H., 2005. Improved pore network extraction methods. In: International Symposium of the Society of Core Analysts, Toronto, 21–25 August 2005. vol. 2125. pp. 1–11.
Sweeting, M.M., 1973. Karst Landforms. Columbia University Press, New York.
Szymczak, P., Ladd, A.J.C., 2009. Wormhole formation in dissolving fractures. J. Geophys. Res. 114, B06203.
Szymczak, P., Ladd, A.J.C., 2014. Reactive infiltration instabilities in rocks. Part 2. Dissolution of a porous matrix. J. Fluid Mech. 738, 591–630.
Van Cappellen, P., 1996. Reactive surface area control of the dissolution kinetics of biogenic silica in deep-sea sediments. Chem. Geol. 132 (1–4), 125–130.
Voltolini, M., Ajo-Franklin, J., 2019. The effect of CO_2-induced dissolution on flow properties in Indiana Limestone: An in situ synchrotron X-ray micro-tomography study. Int. J. Greenh. Gas Control. 82, 38–47.
Walsh, P., Morawiecka-Zacharz, I., 2001. A dissolution pipe palaeokarst of mid-pleistocene age preserved in miocene limestones near staszów, poland. Palaeogeogr. Palaeoclimatol. Palaeoecol. 174 (4), 327–350.
Weller, H.G., Tabor, G., Jasak, H., Fureby, C., 1998. A tensorial approach to computational continuum mechanics using object-oriented techniques. Comput. Phys. 12 (6), 620–631.
Yu, L., Szymczak, P., Ladd, A.J., 2022. Dissolution of periodic arrays of grains: Upscaling of pore-scale simulations with fast reactions. Chem. Geol. 592, 120687.